arXiv:1512.08781v1 [cond-mat.mtrl-sci] 29 Dec 2015

A strongly robust topological Weyl fermion semimetal state in Ta_3S_2

Guoqing Chang*,[1,2,3] Su-Yang Xu*†,[3] Daniel S. Sanchez,[3] Shin-Ming Huang,[1,2,3] Chi-Cheng Lee,[1,2] Tay-Rong Chang,[4,3] Hao Zheng,[3] Guang Bian,[3] Ilya Belopolski,[3] Nasser Alidoust,[3] Horng-Tay Jeng,[4,5] Arun Bansil,[6] Hsin Lin†,[1,2] and M. Zahid Hasan†[3]

[1]*Centre for Advanced 2D Materials and Graphene Research Centre National University of Singapore, 6 Science Drive 2, Singapore 117546*

[2]*Department of Physics, National University of Singapore, 2 Science Drive 3, Singapore 117542*

[3]*Laboratory for Topological Quantum Matter and Spectroscopy (B7), Department of Physics, Princeton University, Princeton, New Jersey 08544, USA*

[4]*Department of Physics, National Tsing Hua University, Hsinchu 30013, Taiwan*

[5]*Institute of Physics, Academia Sinica, Taipei 11529, Taiwan*

[6]*Department of Physics, Northeastern University, Boston, Massachusetts 02115, USA*

(Dated: December 31, 2015)

* These authors contributed equally to this work.

† Corresponding authors: suyangxu@princeton.edu, nilnish@gmail.com, and mzhasan@princeton.edu

Abstract

Weyl semimetals are extremely interesting because they provide the first realization of the Weyl fermion, expand the classification of topological phases beyond band insulators, exhibit exotic quantum anomalies, and host novel Fermi arc surface states. Although the first Weyl semimetal was recently discovered in TaAs, research progress on this newly discovered topological phase is still significantly hindered due to the lack of robust and ideal materials candidates. In order to observe the many predicted exotic phenomena that arise from Weyl fermions, it is of critical importance to find robust and ideal Weyl semimetals, which have fewer Weyl nodes and more importantly whose Weyl nodes are well separated in momentum space and are located close to the chemical potential in energy. In this paper, we propose by far the most robust and ideal Weyl semimetal candidate in the inversion breaking, single crystalline compound tantalum sulfide Ta_3S_2 with new and novel properties beyond TaAs. We find that Ta_3S_2 has only 8 Weyl nodes, all of which have the same energy that is merely 10 meV below the chemical potential. Crucially, our results show that Ta_3S_2 has the largest k-space separation between Weyl nodes among known Weyl semimetal candidates, which is about twice larger than TaAs and twenty times larger than the predicted value in WTe_2. Moreover, we predict that increasing the lattice by $< 4\%$ can annihilate all Weyl nodes, driving a novel topological metal-to-insulator transition from a Weyl semimetal state to a topological insulator state. We further discover that changing the lattice constant also serves as a powerful way to tune the energy of Weyl fermion bands with respect to the chemical potential. Both the Weyl nodes and the van Hove singularities with enhanced density of states can be moved to the chemical potential depending the change of the lattice constant. Our prediction provides a critically needed robust candidate for this rapidly developing field. The well separated Weyl nodes, the topological metal-to-insulator transition and the remarkable tunabilities suggest Ta_3S_2's potential as the ideal platform in future device-applications based on Weyl semimetals.

The rich correspondence between high-energy particle physics and low-energy condensed matter physics has been a constant source of inspiration throughout the history of modern physics [1]. This has led to important breakthroughs in many aspects of fundamental physics such as the Planck constant and the blackbody radiation, the Pauli exclusion principle and magnetism, as well as the Anderson-Higgs mechanism and superconductivity, which in turn helped us understand materials leading to important practical applications. Recently, there has been significant interest in realizing high energy particles in solid state crystals. The discovery of massless Dirac fermions in graphene and on the surface of topological insulators has taken center stage of the past decade's research in condensed matter and materials science [2–5]. Weyl semimetals [6–21] are crystals whose quasiparticle excitation is the Weyl fermion [6], a particle that played a crucial role in the development of quantum field theory and the Standard Model but has not yet been observed as a fundamental particle in Nature. Weyl fermions have a definite left- or right-handed chirality, and can be combined in pairs of opposite chirality to generate a massless Dirac fermion. In a Weyl semimetal, the chirality associated with each Weyl node can be understood as a topologically protected charge, hence broadening the classification of topological phases of matter beyond insulators. Interestingly, the presence of parallel electric and magnetic fields can break the apparent conservation of the chiral charge, which results in the condensed matter version of the chiral anomaly, making a Weyl semimetal, unlike ordinary nonmagnetic metals, more conductive with an increasing magnetic field [22, 23]. Remarkably, Weyl nodes are extremely robust against imperfections in the host crystal, and are protected by the crystals inherent translational invariance [12]. This gives rise to an exceptionally high electron mobility, suggesting that Weyl semimetals may be used to improve electronics by carrying electric currents more efficiently [24]. Because Weyl fermion quasiparticles are naturally spin-momentum locked [12, 14, 15] and superconductivity in these materials may exhibit non-Abelian statistics [25–27], they may also be exploited to realize new applications, such as in spintronics and quantum computers. Furthermore, the nontrivial topology guarantees an exotic boundary mode, the Fermi arc surface state [16, 19]. Such band structure would violate quantum mechanics in any purely 2D electron system, but uniquely allowed in a Weyl semimetal because pairs of Weyl fermions with opposite chirality are connected through the boundary of the crystal. Because of these novel properties, Weyl semimetals have the potential to be as important as graphene and topological insulators.

Despite the immense interest, for many years, the Weyl semimetal remained a purely theoretical concept. Early this year, the first Weyl semimetal was discovered in the TaAs family [17–19, 21, 28–37]. However, research progress is still significantly held back due to the lack of robust and ideal materials candidates. In a Weyl semimetal, Weyl nodes of opposite chirality are separated in momentum space. The degree of separation between Weyl nodes provides a measure of the Weyl phase's "topological strength" [38] that one has to overcome in order to annihilate the Weyl fermions in pairs. A large k space separation of the Weyl nodes gurantees a robust and stable Weyl semimetal state, which is the prerequisite for observing the many exotic phenomena predicted to be detectable in spectroscopic and transport experiments. Therefore, finding Weyl semimetals with well separated Weyl nodes is of critical importance.

In this paper, we propose by far the most robust Weyl semimetal candidate in the inversion breaking, single crystalline compound tantalum sulfide Ta_3S_2, which exhibits new and novel properties beyond those found in TaAs. Specifically, we find that Ta_3S_2 has only 8 Weyl nodes, significantly simpler than the 24 Weyl nodes in TaAs. All 8 Weyl nodes in Ta_3S_2, contrary to TaAs, have the same energy that is merely 10 meV below the chemical potential. Our results clearly demonstrate that Ta_3S_2 has the largest k-space separation between Weyl nodes among the known Weyl semimetal candidates, which is about twice larger than the measured value in TaAs [19] and twenty times larger than the predicted value in WTe_2 [41]. This is crucially important for both observing the Weyl nodes in spectroscopic measurements and for probing the chiral anomaly and other monopole physics in transport experiments. Moreover, we predict that increasing the lattice constant by ¡4% will result in the annihilation of all the Weyl nodes in Ta_3S_2 and, consequently, drive a novel topological metal-to-insulator transition from a Weyl semimetal state to a topological insulator state. Such a transition is imperative for raising our understanding of the nontrivial topology of the Weyl semimetal state because it is predicted to be an intermediate phase between a trivial and a topological insulator states [11]. However, this prediction has never been experimentally demonstrated. This transition is also relevant for potential future applications because the ability to open up a band gap is necessary for many practical purposes such as building a transistor. We also find that increasing the lattice constant serves as a powerful way to effectively tune the energy of Weyl fermion bands, with respect to the chemical potential. Both the Weyl nodes and the van Hove singularities arising from the Weyl fermion cones

can be moved to the chemical potential via changing the lattice constant. Finally, we show that the Weyl nodes in Ta_3S_2 arise from a new type of critical point that is distinct from any known Weyl semimetal candidate system. These properties not only identify Ta_3S_2 as the most robust Weyl semimetal candidate to date but also suggest its potential in transport and future device applications.

Ta_3S_2 crystalizes in a base-centered orthorhombic structure [39, 40]. Single crystals of this compound has been grown [39, 40], and transport experiments indeed reported a semimetallic behavior [40]. The lattice constants are $a = 5.6051$Å, $b = 7.4783$Å and $c = 17.222$Å, and the space group $Abm2$ (#39). There are 24 Ta atoms and 16 S atoms in a conventional unit cell (Figs. 1**a,b**). It can be seen that the lattice lacks space-inversion symmetry, which is key to realizing the Weyl semimetal state in this time-reversal invariant system. Moreover, the system has two glide mirror symmetries associated with the y and z directions, i.e., $\mathcal{G}_y$: $(x, y, z) \Rightarrow (x, -y, z+0.5)$ and $\mathcal{G}_z : (x, y, z) \Rightarrow (x, y, -z+0.5)$, but it does not have any mirror symmetry along the x direction. The symmetry condition determines the number, energy and momentum space configuration of the Weyl nodes in Ta_3S_2, which will be discussed below.

Figs.1**d,f** shows the first-principles calculated band structure in the absence of spin-orbit coupling (SOC), from which it can be seen that the conduction and valence bands dip into each other, suggesting a semimetallic ground state. Particularly, we find that the conduction and valence bands cross each other without opening up a gap along the $\Gamma - X - Z - X_1$ direction. Upon the inclusion of SOC (Figs.1**e,g**), the band structure is found to be fully gapped along all high symmetry directions.

In order to search for the Weyl nodes in Ta_3S_2, we calculated the band structure throughout its Brillouin zone (BZ). In the absence of SOC (Fig.2**a**), we found a line node on the $k_y = 0$ plane, which is the band crossings along $\Gamma - X - Z - X_1$ direction as seen in Fig.1**d**. We note that this line node is on the $k_y = 0$ plane and is,therefore, protected by the mirror symmetry $\mathcal{G}_y$. In addition, we also found two pairs of Weyl nodes located on the $k_x = 0$ plane (Fig.2**a**). We determine the chirality of the Weyl node by computing the Berry curvature through a closed 2D manifold enclosing the node. Considering the available symmetries as discussed above, Ta_3S_2 has only one irreducible pair of Weyl nodes. The second pair is obtained by applying the Mirror operation $\mathcal{G}_z$. In general, a mirror symmetry operation reflects a Weyl node on one side of the mirror plane to the mirror-reflected location on the

other side, while also flipping the sign of the chiral charge. Hence it can be seen that that the two pairs of Weyl nodes without SOC are directly related by the Mirror operation $\mathcal{G}_z$. Upon the inclusion of SOC, each Weyl node without SOC splits into two spinful Weyl nodes of the same chirality. This is quite intuitive because each state without SOC should be considered as two states of opposite spins. For this reason there are four pairs of Weyl nodes in the presence of SOC. Again, there is only one irreducible pair and the others are related by the Mirror operations $\mathcal{G}_y$ and $\mathcal{G}_z$. Also because of the mirror symmetries, all the Weyl nodes have the same energy in Ta_3S_2. We show the dispersion away from a Weyl node along all three momentum space directions in Figs.2**c,d**. It can be seen that Ta_3S_2's Weyl nodes are of the so-called type II [41] because the two bands that cross to form the Weyl nodes have the same sign of velocity along one momentum direction (in this case, k_y). In the presence of SOC (Fig.2**d**), the Weyl nodes are approximately 10 meV below the Fermi level, which is in contrast to the case in the $Mo_xW_{1-x}Te_2$ systems [38, 41]. This makes Ta_3S_2 more hopeful than $Mo_xW_{1-x}Te_2$ [38, 41] for observing the type II Weyl nodes by photoemission experiments. More importantly, the k separation of the Weyl nodes (Fig.2**d**) in Ta_3S_2 is as large as ~ 0.15 Å^{-1}. This is by far the largest in known Weyl semimetal candidates, and, in fact, twice larger than the measured value in TaAs (about 0.07 to 0.08 Å^{-1}) [19] and twenty times larger than the predicted value in WTe_2 (~ 0.007 Å^{-1}) [41]. The facts that the Weyl nodes are well-separated in momentum space and that they are located close to the chemical potential make Ta_3S_2 the by far most robust and ideal Weyl semimetal candidate for observing and realizing the novel Weyl physics in both spectroscopic and transport experiments.

Another signature of the Weyl semimetal state is the Fermi arc electron states on the surface of the crystal. Figure 3 shows the calculated surface state electronic structure on Ta_3S_2's $(\bar{2}02)$ surface. The calculated surface Fermi surface (Figs. 3**a,d**) show a rich structure, including both topological Fermi arcs and topologically-trivial surface states. There are finite projected bulk Fermi surfaces as shown by the shaded areas in Fig. 3**d**, because the all Weyl nodes are type II. It is known that, at the energy of a type II Weyl node, the bulk Fermi surface is not an isolated point but a touching point between an electron and a hole pockets [41]. It is interesting to note that the surface Fermi surface does not respect mirror symmetry along the $\bar{\Gamma}-\bar{X}$ or $\bar{\Gamma}-\bar{Y}$ axis. As seen from Fig. 1**b**, the $\bar{\Gamma}-\bar{Y}$ is the projection of the $k_x = 0$ plane, which is not a mirror plane. The $\bar{\Gamma}-\bar{X}$ is the projection

of the $k_y = 0$ plane, which is indeed a mirror plane. However, it corresponds to a glide mirror operation, $\mathcal{G}_y : (x, y, z) \Rightarrow (x, -y, z + 0.5)$. Therefore, the $(\bar{2}02)$ surface breaks the glide mirror symmetry. To visualize the Fermi arc surface states, Fig. 3**b** shows the energy dispersion cut along the $Cut1$ (defined by the red dotted line in Fig. 3**a**). In both box 1 and box 2, we clearly see that a surface state is terminated directly onto a Weyl node, which is the touching point between the shaded areas. This calculation demonstrates the existence of the Fermi arc surface states. Specifically, we label the two surface states in the box 1 (upper right panel in Fig. 3**b**) as β and α from left to right. We see that β is the Fermi arc. In Fig. 3**d**, we show the high-resolution Fermi surface zoomed in near the $\bar{X}$ point. The Weyl node that corresponds to the box 1 is the black dot that is directly above the the bottom-left most black dot in Fig. 3**d**. The two surface states, α and β are be identified, and, indeed, the left surface state, β, is the Fermi arc terminating onto this Weyl node. Through similar analyses, we can determine that α is the Fermi arc corresponding to the bottom-left most Weyl node. Based on the above analyses, we show the determined Fermi arc connection in Fig. 3**e**. We also emphasize that the topological band theory of the Weyl semimetal phase only requires the number of Fermi arcs that are terminated on a given projected Weyl node must equal the absolute value of its chiral charge. The detailed connectivity pattern can vary based on the surface conditions such as the surface potential, surface relaxation, surface density, etc. Hence the purpose of Fig. 3 is to show the existence of the Fermi arcs, which is a key signature of the Weyl semimetal state in Ta_3S_2. The details of the surface electronic structure, including the connectivity pattern, will depend on the surface conditions, which have to be determined by experiments.

Now we show the topological metal to insulator transition in Ta_3S_2 in Fig. 4. In order to best visualize the transition, we show the band dispersion along a cut that goes through an irreducible pair of Weyl node (as defined by the red dotted line in Fig. 5**d**). As shown in Fig. 4**a**, we show this cut as a function of different values of the lattice constant b. At the original lattice constant, $b' = b$, we indeed see a pair of type II Weyl nodes, as expected. As we increase the lattice constant by 3.0%, $b' = 1.030b$, we see that Weyl nodes approach each other and their separation decreases by half. As we further increase the lattice constant to $b' = 1.040b$, the two Weyl nodes annihilate with each other and the band structure become fully gapped. By a careful calculation, we determined that the lattice constant corresponding to the critical point is $b' = 1.037b$. The resulting fully gapped state for $b' > 1.037b$ has two

possible fates, i.e., either being a trivial insulator or being a topological insulator. We have calculated the the Wilson loop of the Wannier function centered on the $k_z = 0$ plane and on the $k_z = \pi$ plane (Fig. 4**b**), from which we determined that the gapped state for $b' > 1.037b$ is a topological insulator and its $\mathcal{Z}_2$ indices are $(1; 000)$. Therefore, by increasing the lattice constant b, one can realize a topological phase transition from a Weyl semimetal state to a topological insulator state in Ta_3S_2. The corresponding evolution of the surface electronic structure is shown in Fig. 4**c** for the case of the $(\bar{2}02)$ surface. Interestingly, the projected Weyl nodes of opposite chirality, which are connected by the Fermi arcs, approach each other and eventually meet on the $\bar{X} - \bar{\Gamma}$ axis where they annihilate. The resulting surface has a single surface state whose Fermi surface encloses the Kramers' point $\bar{X}$, which also demonstrates the topological insulator state.

Besides the topological phase transition, we found that the system exhibits other important tunabilities. Specifically, it can be seen that while the Weyl nodes at the original lattice constant are type II, they become type I at $b' = 1.030b$ because the Weyl node is now formed by two bands with the opposite sign of velocity (Fig. 4**a**). Therefore, interestingly, there is a transition from type II Weyl fermions to type I Weyl femions as one increases the lattice constant b. Moreover, we note that the energy of the bands in Fig. 4**a** shifts across the chemical potential as one increases b. Therefore, there also exist specific values of the lattice constant b, at which important features will be moved exactly onto the chemical potential. We focuses on two important features, i.e., the Weyl nodes and the van Hove singularities (VHS) that arise from the Weyl cones (see middle panel of Fig. 4**a**). Placing the Weyl nodes at the Fermi level is very meaningful because the Weyl nodes are monopoles of Berry curvature. Thus any novel phenomenon that arises from the chirality of the Weyl fermions such as the chiral anomaly will become the most significant when the Weyl nodes are at the Fermi level. Putting the VHS at the Fermi level can also interesting because the VHS is due to a saddle point in the band structure, which means that the density of states will show a maxima at the energy of the VHS. An enhanced density of states is favorable for inducing correlated physics such as superconductivity or magnetism. A detailed phase diagram is shown in Fig. 4**c**.

We show that band structure of Ta_3S_2 exhibits a new type of critical point as one decreases the lattice constant c or increases the spin-orbit coupling λ. As discussed above, at ambient conditions, the conduction and valence bands only touch each other at 8 discrete points in

the BZ, which are the 8 Weyl nodes. Here, we show that decreasing the lattice constant c or increasing the spin-orbit coupling λ leads to the generation of new Weyl nodes. Representing the critical point for this process is the critical value for the lattice constant c or spin-orbit coupling λ corresponding to the point where the conduction and valence bands just touch, $c_{\text{critical}} = 0.98c$ or $\lambda_{\text{critical}} = 1.027\lambda$. Taking the critical point of $\lambda_{\text{critical}} = 1.027\lambda$ as the example, we show the k space locations of these newly emerged band touchings by the green dots in Fig. 5**d**. Interestingly, we find that the critical point band structure is novel. Specifically, the dispersion along k_z near the band touching behaves like two downward facing parabolas. These two parabolas touch at their vertex, which forms the band touching point. This is distinct from the critical points associated with any previously known Weyl semimetal candidates. For example, the critical point band structure of TaAs can be thought of as two parabolas of opposite directions, one facing up and the other facing down (Fig. 5**a**). Then entering the Weyl phase from the critical point essentially means "pushing" the two parabolas "into" each other so that they cross to form the two Weyl nodes. The situation in the $Mo_xW_{1-x}Te_2$ system is very similar, but the only difference is that the direction of the parabolas is titled away from being vertical (Fig. 5**b**). By contrast, in Ta_3S_2 we have two parabolas that face the same direction (Fig. 5**c**). A distinct and unique property of the new critical point is that it leads to a saddle point in the band structure, giving rise to a van Hove singularity. The saddle point behavior can be seen from the band dispersions shown in Fig. 5**e**. If one focuses on the conduction band in Fig. 5**e**, the touching point is the energy minima for the dispersions along the k_x, k_y directions but it is the energy maxima along the k_z direction. The saddle point band structure brings about a van Hove singularity, which generates a maxima in the density of states (DOS) and a divergence in the first derivative of the DOS at the energy of the van Hove singularity, as seen in Fig. 5**g**.

We discuss the meaning of the **robust** and **ideal** Weyl semimetal candidate as emphasized in our paper. Firstly, we mean that the realization of the candidate is likely to be experimentally feasible. This involves the following critical conditions: (1) The prediction is based on the realistic crystal structure, meaning that the compound does crystalize in the proposed crystal structure at ambient conditions. (2) The prediction does not require fine tuning of the chemical composition or the magnetic domains. (3) The Weyl nodes are not located at energies far above the chemical potential so that they can be observed by photoemission. This was the case for our prediction of TaAs [17], which has now been realized [19].

This is also the case here for Ta_3S_2, which demonstrates that the experimental feasibility of our proposal on Ta_3S_2. Secondly, and more importantly, the term "robust" also refers to a large separation of the Weyl nodes in momentum space because, as discussed above, the separation of the Weyl nodes provides a measure of a Weyl semimetal's topological strength. We highlight again that Ta_3S_2 has the largest k-space separation between Weyl nodes among known Weyl semimetal candidates, which is about twice larger than TaAs. This will greatly help resolve the Weyl nodes in various spectroscopic measurements such as photoemission and scanning tunneling spectroscopies. This will also make it easier to probe the chiral anomaly and other monopole physics in electrical and optical transport experiments.

Finally, in order to facilitate the topological metal-to-insulator transition that we predict in Ta_3S_2, we propose the following three methods for changing the b lattice constant: (1) applying external pressure, (2) growing Ta_3S_2 film onto a substrate with lattice mismatch, and (3) growing samples with isoelectronic chemical substitution such as $Ta_3(S_{1-x}Se_x)_2$ or $(Ta_{1-x}Nb_x)_3S_2$. We also compare the topological metal-to-insulator transition in Ta_3S_2 with transitions predicted in other Weyl candidates to highlight the superior feasibility of our proposal [42, 43]. A theoretical work [42] predicted the topological phase transitions from a trivial band insulator to a Weyl semimetal and then to a topological insulator by varying the chemical composition x in $LaBi_{1-x}Sb_xTe_3$ or applying external pressure to BiTeI. However, the composition or pressure range that corresponds to Weyl semimetal phase is predicted to be extremely narrow [42]. Hence it requires ultra-fine tuning, which is very difficult in experiments. Also, $LaBi_{1-x}Sb_xTe_3$ has never been grown in the crystal structure required by the proposal [42] at least in the single crystal form. Another work [43] proposed similar transitions in the β-Bi_4Br_4 under external pressure. In order to induce a Weyl semimetal phase in the β-Bi_4Br_4 crystal structure that does have inversion symmetry, a hypothetical inversion breaking term was assumed in the calculation. By contrast, Ta_3S_2 is an inversion breaking, single crystalline compound. Single crystalline Ta_3S_2 samples have been grown [39, 40]. The Weyl semimetal state is stable and does not require fine tuning. These facts highlight that Ta_3S_2 is, to date, not only the most ideal platform for advancing our understanding of Weyl semimetals and Weyl physics, but to also facilitate the exploitation of the exotic and novel properties in future device applications.

METHODS

First-principles calculations of Ta_3S_2 were performed by the OpenMX code based on norm-conserving pseudopotentials generated with multi-reference energies and optimized pseudoatomic basis functions [44, 45]. The spin-orbit coupling was incorporated through j-dependent pseudo-potentials, and the generalized gradient approximation was adopted for the exchange-correlation energy functional [46, 47]. For each Ta atom, three, two, two, and one optimized radial functions were allocated for the s, p, d and f orbitals ($s3p2d2f1$), respectively. For each S atom, $s3p3d2f1$ was adopted. The cut off radius for both Ta and S basis functions was 7 Bohr, and the cut-off energy was 1000 Ry. A k point mesh of $(13 \times 11 \times 11)$ for the primitive unit cell and the experimental lattice parameters were adopted in the calculations. We used the Ta d and S p orbitals to construct the Wannier functions. We calculated the surface spectral weight of a semi-infinite $(\bar{2}02)$ slab using the iterative Green's function method from the Wannier function based Tight-binding model. We did not choose the (001) and the (010) surfaces because pairs of Weyl nodes of opposite chirality are projected onto each other on these two surfaces (Fig.2**b**). Hence the (001) and the (010) surfaces do not carry net projected chiral charge and are not expected to show Fermi arcs. Because the purpose of the surface calculations (Fig. 3) was to demonstrate the existence of Fermi arcs, the usage of the $(\bar{2}02)$ surface is proper and sufficient.

[1] Wilczek, F. Why are there Analogies between Condensed Matter and Particle Theory? *Phys. Today* **51**, 11-13 (1998).

[2] Geim, A. K. and Novoselov, K. S. The rise of graphene. *Nature Mater.* **6**, 183-191 (2007).

[3] Hasan, M. Z. and Kane, C. L. Colloquium: Topological insulators. *Rev. Mod. Phys.* **82**, 3045-3067 (2010).

[4] Qi, X.-L. and Zhang, S.-C. Topological insulators and superconductors. *Rev. Mod. Phys.* **83**, 1057-1110 (2011).

[5] Hasan, M. Z. and Moore, J. E. Three-Dimensional Topological Insulators. *Ann. Rev. Cond. Mat. Phys.* **2**, 55-78 (2011).

[6] Weyl, H., Elektron und gravitation. *Z. Phys.* **56**, 330-352 (1929).

[7] Herring, C. Accidental Degeneracy in the Energy Bands of Crystals. *Phys. Rev.* **52**, 365-373

(1937).

[8] Abrikosov, A. A. and Beneslavskii, S. D. Some Properties of Gapless Semiconductors of the Second Kind. *J. Low Temp. Phys.* 5, 141-154 (1972).

[9] Nielsen, H. B. and Ninomiya, M. The Adler-Bell-Jackiw anomaly and Weyl fermions in a crystal *Phys. Lett. B* **130**, 389-396 (1983).

[10] Volovik, G. E. *The Universe in a Helium Droplet* (Oxford University Press, 2003).

[11] Murakami, S. Phase transition between the quantum spin Hall and insulator phases in 3D: emergence of a topological gapless phase. *New J. Phys.* **9**, 356 (2007).

[12] Wan, X., Turner, A. M., Vishwanath, A., and Savrasov, S. Y. Topological semimetal and Fermi-arc surface states in the electronic structure of pyrochlore iridates. *Phys. Rev. B* **83**, 205101 (2011).

[13] Yang, K.-Y., Lu, Y.-M., and Ran, Y. Quantum Hall effects in a Weyl semimetal: Possible application in pyrochlore iridates. *Phys. Rev. B* **84**, 075129 (2011).

[14] Balents, L. Weyl electrons kiss. *Physics* **4**, 36 (2011).

[15] Burkov, A. A. and Balents, L. Weyl Semimetal in a Topological Insulator Multilayer. *Phys. Rev. Lett.* **107**, 127205 (2011).

[16] Xu, S.-Y. *et al.* Observation of Fermi arc surface states in a topological metal. *Science* **347**, 294-298 (2015).

[17] Huang, S.-M. *et al.* A Weyl Fermion semimetal with surface Fermi arcs in the transition metal monopnictide TaAs class. *Nature Commun.* **6**, 7373 (2015).

[18] Weng, H., Fang, C., Fang, Z., Bernevig, A., and Dai, X., Weyl Semimetal Phase in Noncentrosymmetric Transition-Metal Monophosphides. *Phys. Rev. X* **5**, 011029 (2015).

[19] Xu, S.-Y *et al.* Discovery of a Weyl fermion semimetal and topological Fermi arcs. *Science* **349**, 613-617 (2015).

[20] Lu, L. *et al.* Experimental observation of Weyl points *Science* **349**, 622-624 (2015).

[21] Lv, B. Q. *et al.* Experimental Discovery of Weyl Semimetal TaAs. *Phys. Rev. X* **5**, 031013 (2015).

[22] Huang, X. *et al.* Observation of the chiral anomaly induced negative magneto-resistance in 3D Weyl semi-metal TaAs. *Phys. Rev. X* **5**, 031023 (2015).

[23] Zhang, C. *et al.* Observation of the Adler-Bell-Jackiw chiral anomaly in a Weyl semimetal. Preprint at http://arxiv.org/abs/1503.02630 (2015).

[24] Zhang, C. *et al.* Tantalum Monoarsenide: an Exotic Compensated Semimetal. Preprint at http://arxiv.org/abs/1502.00251 (2015).

[25] Hosur, P. & Qi, X.-L. Time-reversal invariant topological superconductivity in doped Weyl semimetals.*Phys. Rev. B.* **90**, 045130 (2014).

[26] Bednik, G., Zyuzin, A. A. & Burkov, A. A. Superconductivity in Weyl semimetals. *Phys. Rev. B.* **92**, 035153 (2015).

[27] Li, Y. & Haldane, F. D. M. Topological nodal Cooper pairing in doped Weyl seimetals. Preprint at http://arxiv.org/abs/1510.01730 (2015).

[28] Lv, B. Q. *et al.* Observation of Weyl nodes in TaAs. *Nature Phys.* **11**, 724-727 (2015).

[29] Yang L. X. *et al.* Weyl semimetal phase in the non-centrosymmetric compound TaAs. *Nature Phys.* **11**, 728-732 (2015).

[30] Xu, S.-Y. *et al.* Discovery of a Weyl fermion state with Fermi arcs in niobium arsenide. *Nature Phys.* **11**, 748-755 (2015).

[31] Xu, N. *et al.* Observation of Weyl nodes and Fermi arcs in TaP. Preprint at http://arxiv.org/abs/1507.03983 (2015).

[32] Xu, S.-Y. *et al.* Experimental discovery of a topological Weyl semimetal state in TaP. *Science Advances* **1**, e1501092 (2015).

[33] Xu, D. F. *et al.* Observation of Fermi Arcs in non-Centrosymmetric Weyl Semi-metal Candidate NbP. Preprint at http://arxiv.org/abs/1509.03847 (2015).

[34] Belopolski, I. *et al.* Observation of surface states derived from topological Fermi arcs in the Weyl semimetal NbP. Preprint at http://arxiv.org/abs/1509.07465 (2015).

[35] Souma, S. *et al.* Direct Observation of Nonequivalent Fermi-Arc States of Opposite Surfaces in Noncentrosymmetric Weyl Semimetal NbP. Preprint at http://arxiv.org/abs/1510.01503 (2015).

[36] Liu, Z. K. *et al.* Evolution of the Fermi surface of Weyl semimetals in the transition metal pnictide family. *Nature Mater.* **15**, 27-31 (2016).

[37] Zheng, H. *et al.* Atomic Scale Visualization of Quantum Interference on a Weyl Semimetal Surface by Scanning Tunneling Microscopy/Spectroscopy. Preprint at http://arxiv.org/abs/1511.02216 (2015).

[38] Chang, T.-R. *et al.* Arc-tunable Weyl Fermion metallic state in $Mo_xW_{1-x}Te_2$. Preprint at http://arxiv.org/abs/1508.06723 (2015).

[39] Kim, S., Nanjundaswamy, K. S., and Hughbanks, T. *Inorg. Chem.* ***Single-crystal*** structure of tantalum sulfide (Ta_3S_2). Structure and bonding in the Ta_6Sn ($n = 1, 3, 4, 5$) pentagonal-antiprismatic chain compounds. *Inorg. Chem.* **30**, 159-164 (1991).

[40] Nozaki, H., Hiroaki, W., and Takekawa, S. Galvanomagnetic Properties of Ta_3S_2, Ta_2S and Ta_6S. *J. Phys. Soc. Japan* **60**, 3510-3515 (1991).

[41] Soluyanov, A. A. *et al.* Type-II Weyl semimetals. *Nature* **527**, 495-498 (2015)

[42] Liu, J. & Vanderbilt, D. Weyl semimetals from noncentrosymmetric topological insulators. *Phys. Rev. B* **90**, 155316 (2014).

[43] Liu, C.-C., Zhou, J.-J., Yao, Y., and Zhang, F., Weak Topological Insulators and Composite Weyl Semimetals: β-Bi_4X_4 (X=Br, I). Preprint at http://arxiv.org/abs/1509.07183 (2015).

[44] Ozaki, T. Variationally optimized atomic orbitals for large-scale electronic structures. **Phys. Rev. B 67**, 155108 (2003).

[45] Ozaki, T. *et al.* OpenMX V.3.7 (2013) http://www.openmx-square.org.

[46] Theurich, G. & Hill, N. A. Self-consistent treatment of spin-orbit coupling in solids using relativistic fully separable *abinitio* pseudopotentials. **Phys. Rev. B 64**, 073106 (2001).

[47] Perdew, J. P., Burke, K., and Ernzerhof, M., Generalized Gradient Approximation Made Simple. *Phys. Rev. Lett.* **77**, 3865-3868 (1996).

ACKNOWLEDGEMENTS

Work at Princeton University were supported by the by the U.S. Department of Energy (DOE), Office of Science, Basic Energy Sciences (BES) under DE-FG-02-05ER46200. Work at the National University of Singapore was supported by the National Research Foundation (NRF), Prime Ministers Office, Singapore, under its NRF fellowship (NRF award no. NRF-NRFF2013-03). T.-R.C. and H.-T.J. were supported by the National Science Council, Taiwan. H.-T.J. also thanks the National Center for High-Performance Computing, Computer and Information Network Center National Taiwan University, and National Center for Theoretical Sciences, Taiwan, for technical support. The work at Northeastern University was supported by the U.S. DOE/BES grant number DE-FG02-07ER46352, and benefited from Northeastern University's Advanced Scientific Computation Center (ASCC) and the NERSC supercomputing center through DOE grant number DE-AC02-05CH11231. S.M.H., G.C., and T.R.C acknowledge

their visit scholar positions at Princeton University, which were funded by the Gordon and Betty Moore Foundations EPiQS Initiative through Grant GBMF4547 (Hasan).

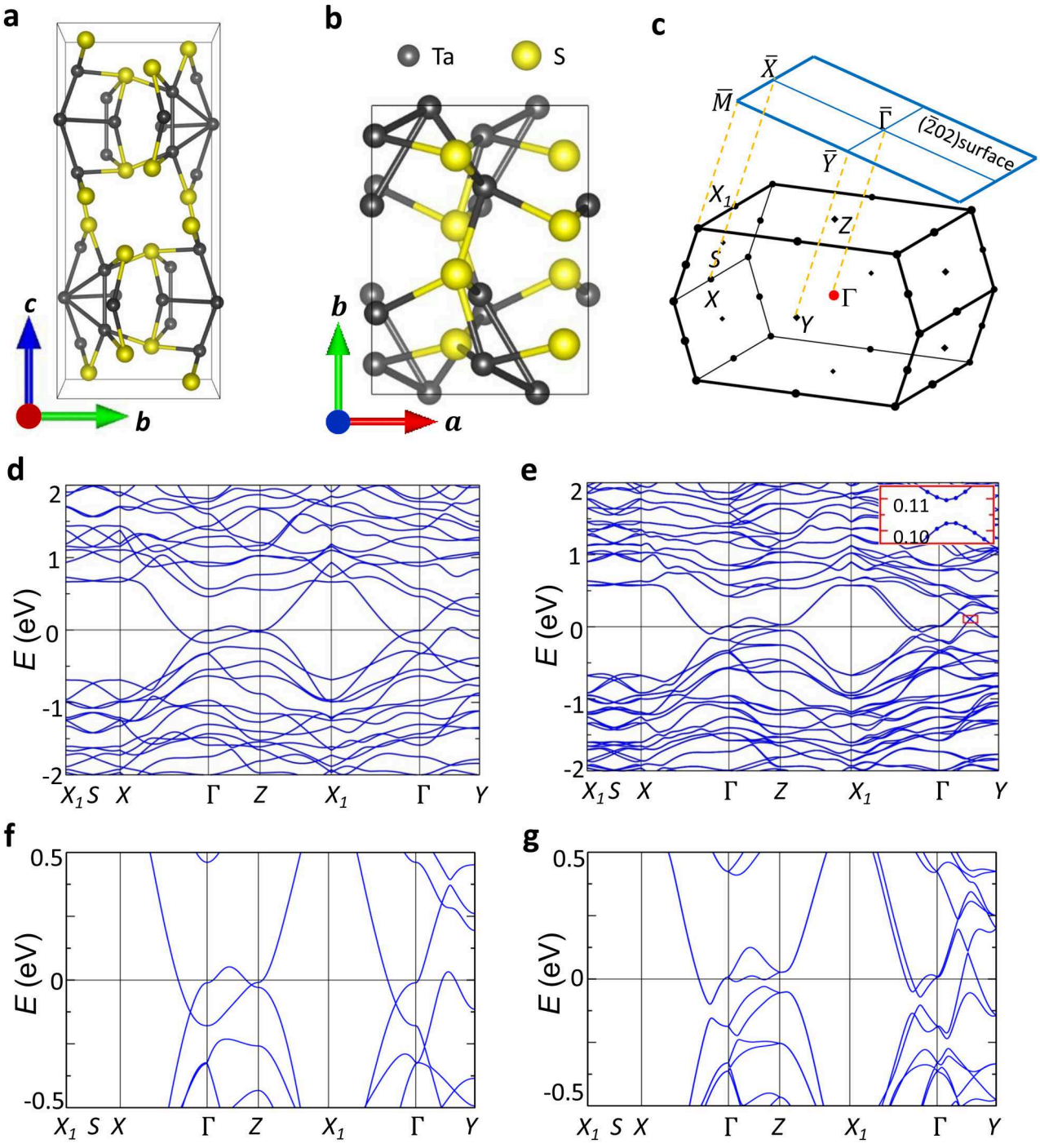

FIG. 1: **Crystal and band structure of Ta_3S_2. a,** Side view of the crystal structure for one unit cell of Ta_3S_2. The dark-grey and yellow balls represent the Ta and S atoms, respectively. **b,** Same as (a) but for the top view. Ta_3S_2 crystallizes in a base-centered orthorhombic structure with space group $Abm2$ (#39) with lattice constants $a = 10.598$Å, $b = 14.135$Å and $c = 32.564$Å. As can be seen from the crystal lattice structure, Ta_3S_2 lacks inversion symmetry.

FIG. 1: **c,** The primitive first Brillouin zone of Ta_3S_2 showing a base-centered orthorhombic structure and the location of relevant high-symmetry points. Representing the $(\bar{2}02)$ surface is a blue rectangular plane. The yellow dashed lines represent the projection of high-symmetry points on the $(\bar{2}02)$ surface. **d,** First-principles electronic band structure calculation for Ta_3S_2 with the absence of spin-orbit coupling. Bulk band crossings observed along the Γ-X-Z-X_1 direction line near the Fermi level are a part of a line node on the $k_y = 0$ plane. **e,** Same as (d) but with the addition of spin-orbit coupling. After the incorporation of spin-orbit coupling, the band structure is fully gapped along all high symmetry directions. Zooming into the red box along the Γ-Y direction shows a minimum gap size between the conduction band minimum and valence band maximum of ≈ 7 meV, which is 96.5% smaller than the 200 meV gap observed along the same direction in (d). (**f-g,**) Zooming in close to the Fermi level for (d)-(e), respectively. Upon the inclusion of SOC, we clearly observe that band structure becomes fully gapped along along all high symmetry directions

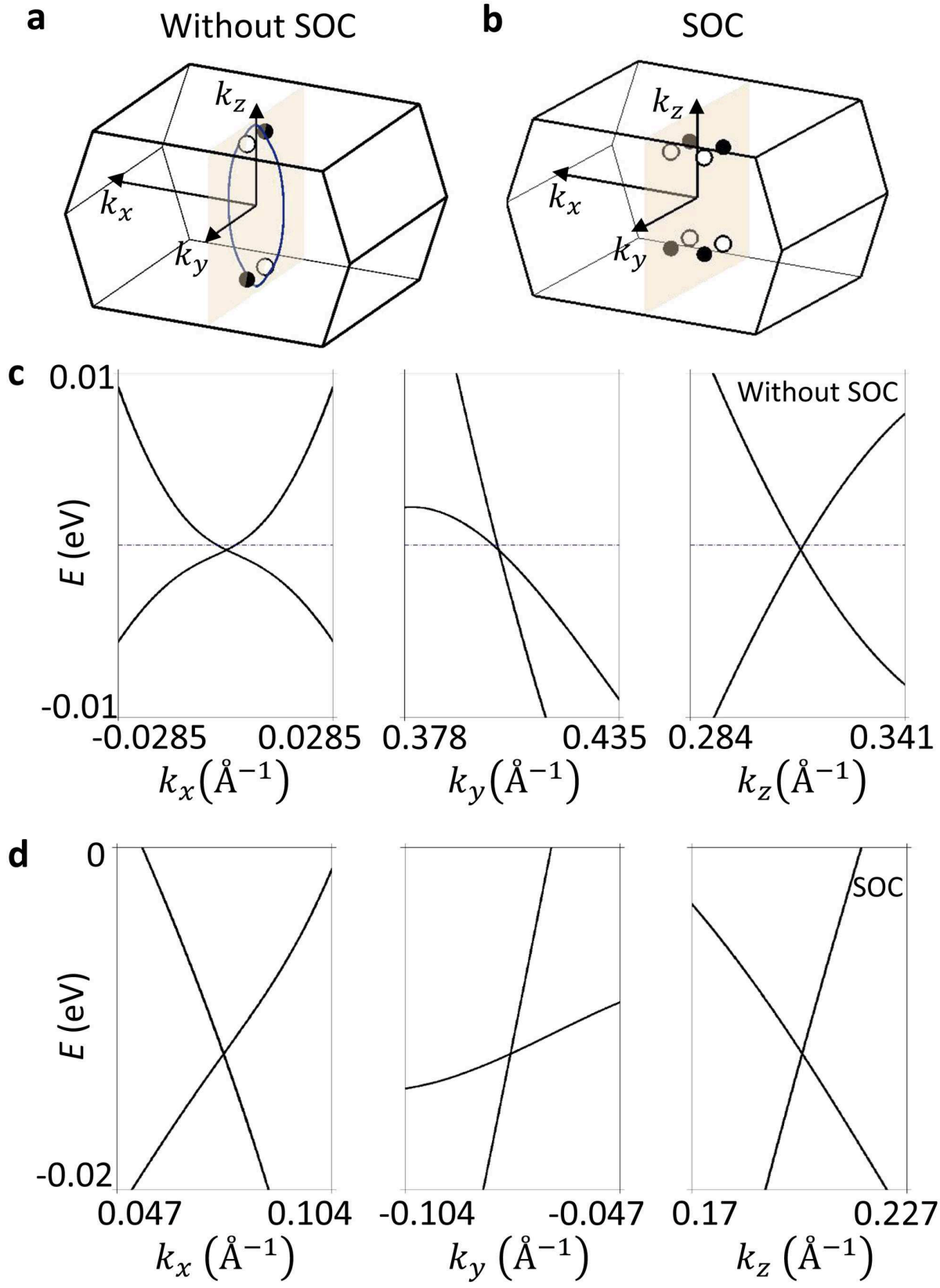

FIG. 2: **Weyl nodes in Ta_3S_2. a,** The primitive first Brillouin zone (BZ) of Ta_3S_2 showing the k-space location of the Weyl points in the absence of spin-orbit coupling.

FIG. 2: The black and white circles represent Weyl points with opposite chirality. On the $k_x = 0$ plane, represented in a tan color, we observe two pairs Weyl nodes with chiral charge ± 1. Only one pair of Weyl nodes is an irreducible representation. Shown in blue is the line node on the $k_y = 0$ plane that corresponds to the crossing along the Γ-X-Z-X_1 direction. **b,** Same as (a) but after the incorporation of spin-orbit coupling. Each Weyl node splits into two spinful Weyl nodes of the same chirality and moves into the bulk. Therefore, we observe 8 Weyl nodes in a single BZ. **c,** The energy dispersion along the three momentum space directions of the Weyl node in the absence of spin-orbit coupling. **d,** Same as (c) but with the addition of spin-orbit coupling. From this series of energy dispersion cuts along the three momentum space directions direction around the Weyl point reveals its type II character (i.e. observe in along k_y that both crossing bands have the same sign of velocity along one momentum direction. Furthermore, observe that the Weyl nodes also move deeper in binding energy, ≈ -10 meV.

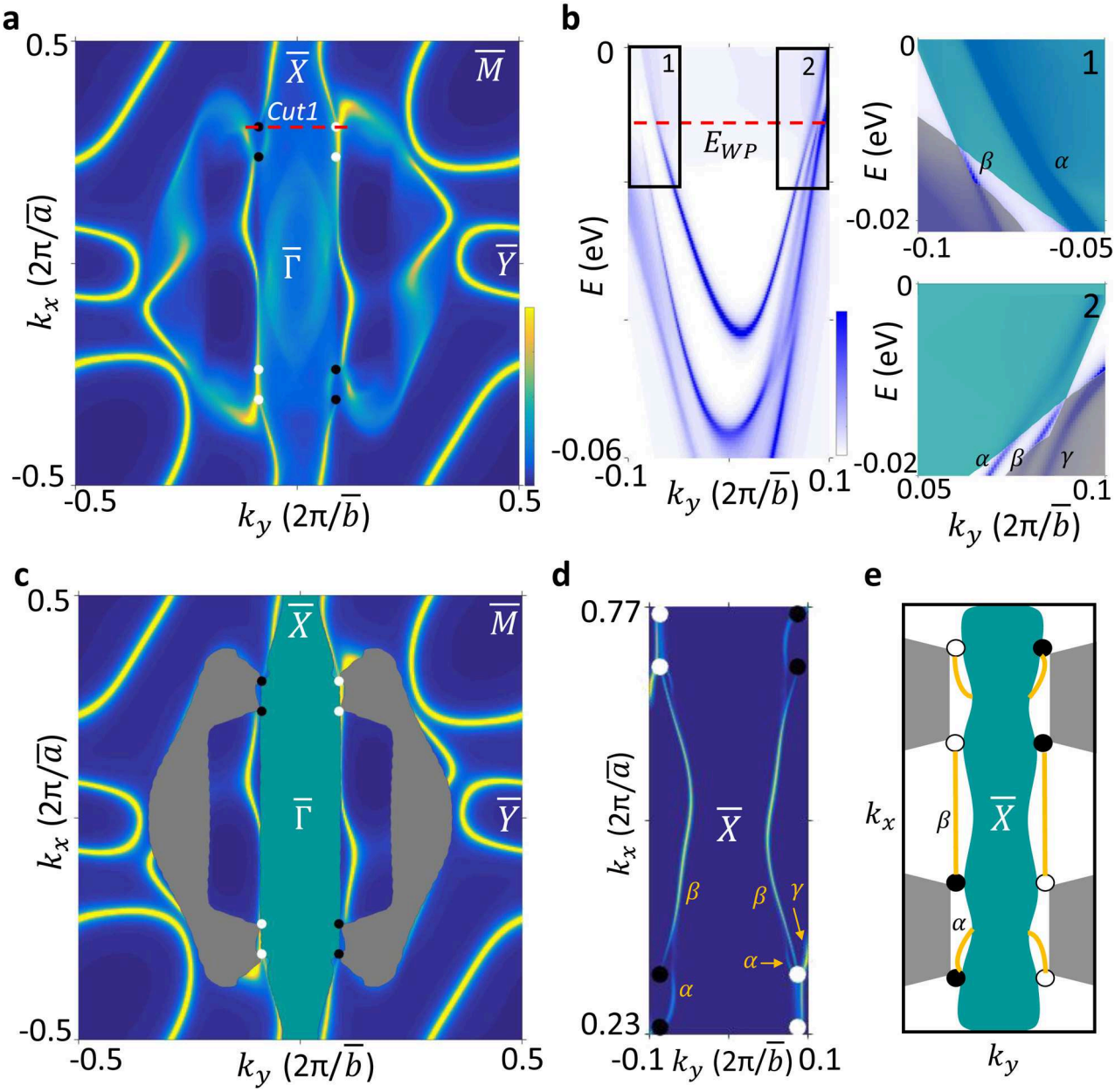

FIG. 3: **Fermi arcs in Ta_3S_2. a,** Surface state spectrum for the $(\bar{2}02)$ surface of Ta_3S_2 at constant energy. Shown in yellow are the surface states. A finite amount of projected bulk Fermi surfaces is observed due to the type II character of the Weyl nodes. Denoted by black and white circles are the projected Weyl nodes. **b,** Energy dispersion cut along Cut1 (red dashed line) for a pair of projected Weyl nodes around $\bar{X}$ in (a). As a guide, the red dashed line represents the energy level of the Weyl node ($E_{W1} \approx -10$ meV). Left panel shows two surface states (blue curves) emerging from box1 and three entering box2. Top-rightmost panel is zoomed into box1 and shows a touching point, which defines the Weyl node as type II, and two Fermi arc surface states that are labeled α and β. The β Fermi arc surface state terminates onto the Weyl node.

FIG. 3: **b,** Bottom-rightmost panel is similar to the top-right most panel. Here we observe three Fermi arc surface states, α, β, and γ. Again, the β Fermi arc surface state is observed to terminate onto the Weyl node. **c,** Same as (a) but with the projected bulk bands represented by shaded areas. The Fermi arc surface states connecting pairs of projected Weyl nodes are distinguishable from the remaining trivial surface states. **d,** Zoom-in of the surface states around the projected Weyl nodes near $\bar{X}$. Shown, among other things, are 8 projected Weyl nodes. Single Fermi arc surface states, β, are shown to connect two individual pairs of Weyl nodes, which is consistent with the predicted ± 1 chiral charge for each Weyl node. The α and γ Fermi arc surface states described in (b) are also labeled. **e,** Cartoon illustration of (d) showing a possible Fermi arc linking scheme. The exact connectivity pattern of Fermi arcs with Weyl nodes depends on the surface conditions.

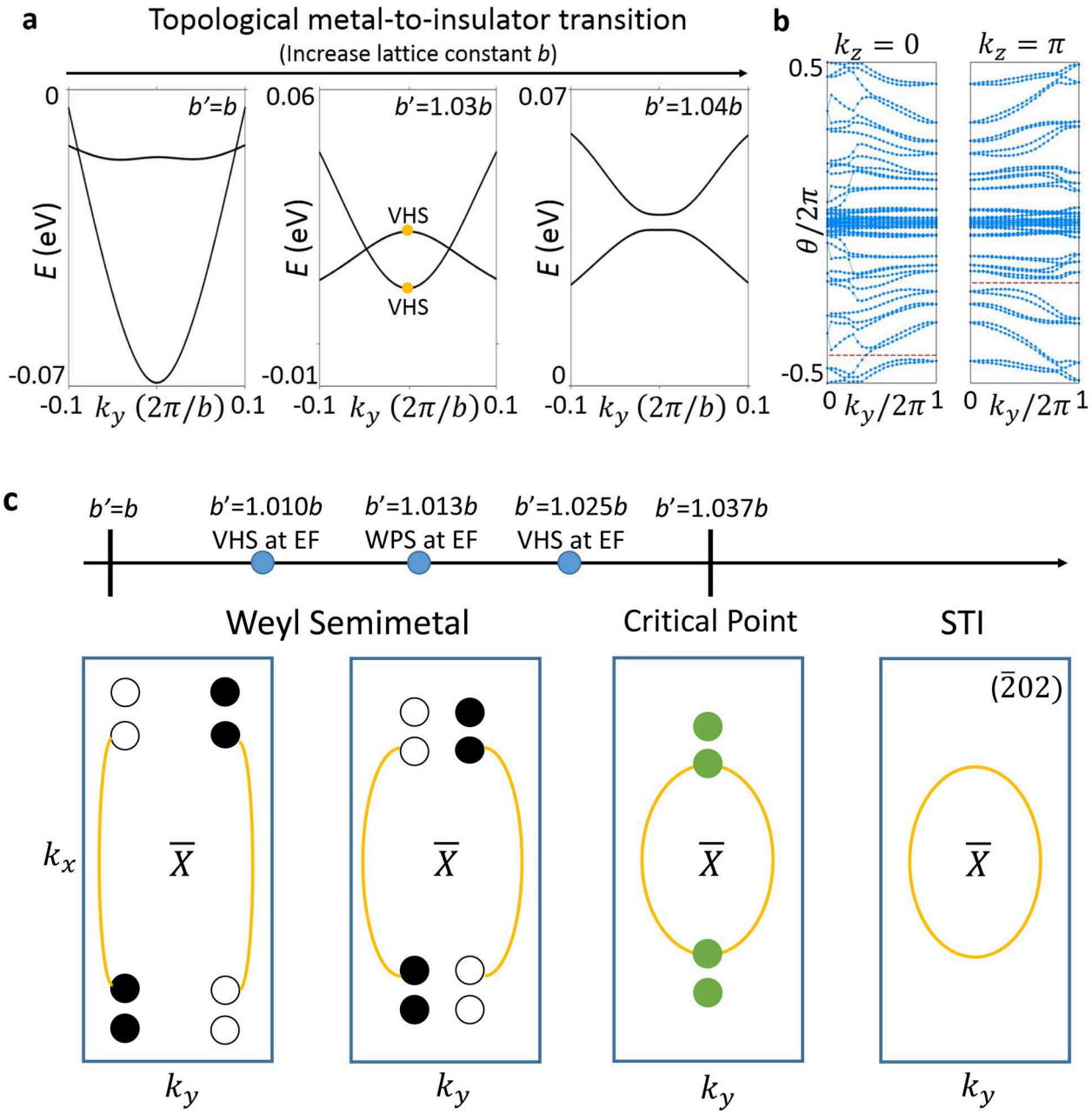

FIG. 4: **Topological metal-to-insulator transition and tunabilities. a,** Energy dispersion cut along k_y for an irreducible pair of Weyl nodes as the b lattice constant is tuned to various values. At the $b' = b$ (left panel) we observe a pair of type II Weyl nodes. At $b' = 1.03b$ (middle panel) the two Weyl nodes approach each other and their separation decreases by about half. Another important feature shown here is the van Hove singularities (VHS), which are labeled with yellow circles. At $b' \geq 1.04b$ (right panel) the two Weyl nodes annihilate each other and the band structure becomes fully gapped. **b,** Calculation of the Wilson loop of the Wannier function centered in the k_z= 0 plane and in the $k_z = \pi$ plane is performed to confirm the strong topological insulator (STI) state. Red-dashed lines are arbitrary reference positions.

FIG. 4: The left panel shows one band crossing the red-dashed line, which corresponds to Z_2 invariant of 1 for k_z=0 plane. The right panel shows no band crossing the red dashed line, which corresponds to Z_2 invariant of 0 for k_z=π plane. Z_2=1 confirms the STI state in Ta_3S_2. **c,** An illustration of the topological metal to insulator transition for the Weyl nodes around the $\bar{X}$ pocket on the $(\bar{2}02)$ surface. Shown in yellow are Fermi arc surface states. As b' is tuned from, the Weyl nodes reach the critical point at $b' = 1.038$ and system becomes fully gapped for $b' > 1.038$ with a single topological surface state with Fermi surface enclosing the Kramers' point $\bar{X}$, resulting a topological insulator state. Furthermore, as b' is tuned from its original value, the van Hove singularities (VHS) arising from the Weyl cone reach the Fermi level when $b' = 1.01b$ and $b' = 1.025b$. The Weyl nodes reach the Fermi level when $b' = 1.013b$.

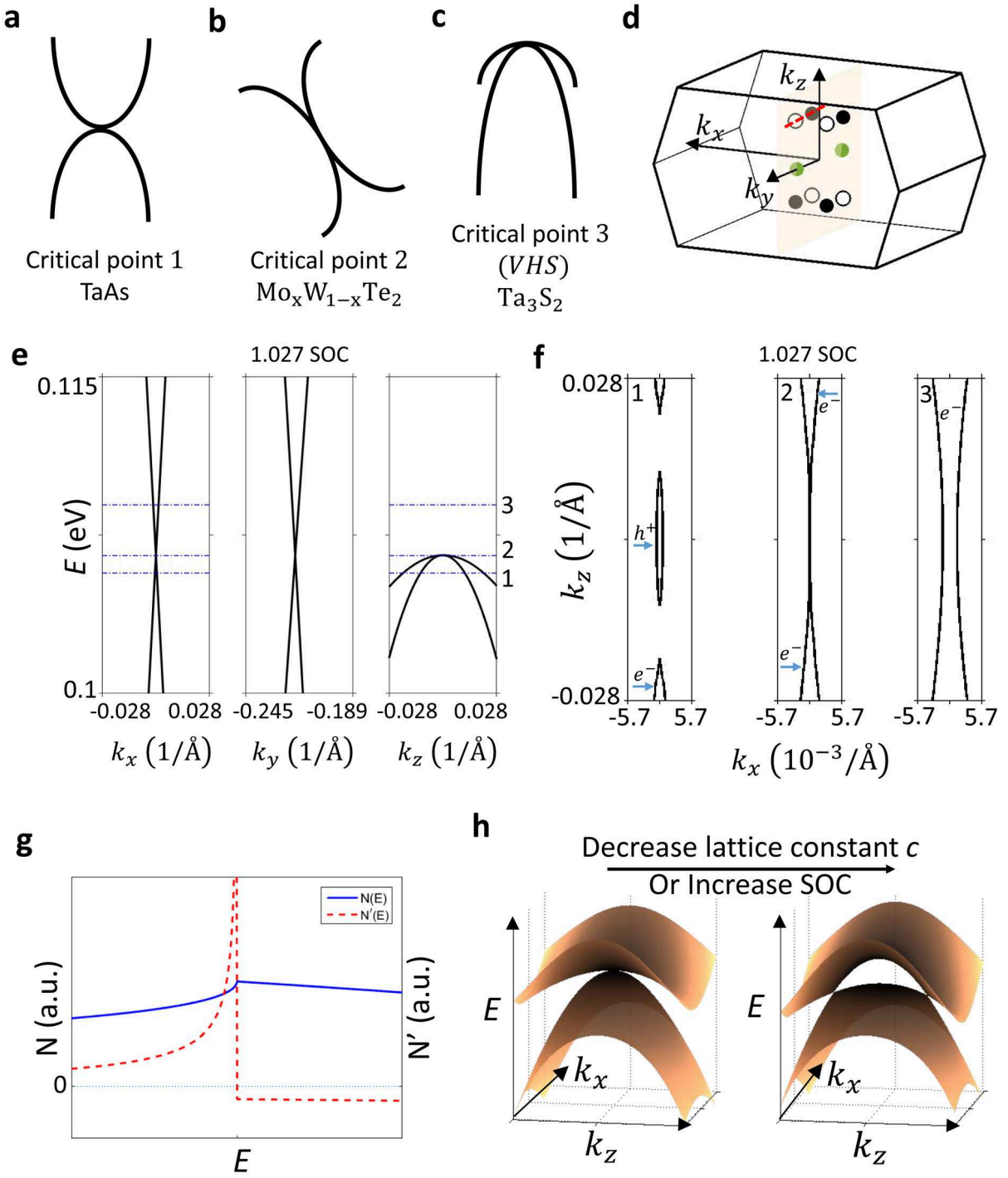

FIG. 5: **A new type of critical point.** **a,** Illustration of the critical point for TaAs as two opposite facing parabolas are driven into each other. **b,** Similar to (a) but for $Mo_xW_{1-x}Te_2$, which shows two oppositely facing parabolas that are tilted away from being vertical. **c,** Ta_3S_2 shows two parabolas that are facing in the same direction. This new type of critical point leads to a saddle point in the band structure and gives rise to a VHS. **d,** The momentum space locations of the newly emerged band touchings resulting from driving the system's

FIG. 5: conduction and valence bands towards each other by changing spin-orbit coupling λ to the critical point $\lambda_{critical} = 1.027\lambda$, which are represented by the green dots. **e,** The saddle point behavior is clearly demonstrated from the band dispersions for $\lambda_{critical} = 1.027\lambda$ by noting that touching point for the conduction band along the k_x and k_y directions is at the energy minimum while being at the energy maximum along the k_z direction. **f,** The Fermi surfaces corresponding to energy levels 1,2, and 3 along the k_x direction in the far-left panel in (e). **g,** The saddle point band structure brings about the VHS, which generates a maxima in the density of states (DOS) (N, blue solid line) and a divergence in the first derivative of the DOS (N', red dashed line) at the energy of the VHS. **h** Illustrations of the conduction and valence bands along the k_z direction as the system is driven to it's critical points by either decreasing the c to $c_{critical}$ lattice constant or increasing the spin-orbit coupling strength λ to $\lambda_{critical}$.